Rare Metal Materials and Engineering
Volume 49, Issue 11, November 2020
Available online at www.rmme.ac.cn

Science Press

Cite this article as: Rare Metal Materials and Engineering, 2020, 49(11): 3761-3768.

ARTICLE

Numerical Simulation of Asymmetrical Fluid Flow and Solidification During the Electron Beam Cold Hearth Re-melting (EBCHR) Process of Titanium Alloy TA10

Xu Yaoping[1], Chen Qipeng[1], Liu Yuan[1], Shi Yaming[2], Qin Tiechang[2], Shen Houfa[1]

[1] Key Laboratory for Advanced Materials Processing Technology, Ministry of Education; School of Materials Science and Engineering, Tsinghua University, Beijing 100084, China; [2] Kunming Iron and Steel Co., Ltd, Kunming 651206, China

Abstract: Fluid flow in the solidifying pool plays an important role for the casting quality in electron beam cold hearth re-melting (EBCHR or EB Re-melting) process. A three-dimensional unsteady state model was built to describe the fluid flow and the sump evolution during the EBCHR process of titanium slab casting. The Mixed Lagrange and Euler (MiLE) approach was employed to investigate the unsteady state casting process. A set of asymmetrical EB power input was tested in the model to demonstrate the characteristic of the fluid flow, temperature distribution and sump profile. The results show that the asymmetrical sump is induced by the coupling of fluid flow and heat transfer within the asymmetrical mold. Part of the inlet fluid infiltrates the solidifying shell, and part of the inlet fluid rebounds to the melt surface. The infiltration of downward inlet flow reduces the solidifying shell, while the rebound of upward inlet flow enforces the heat absorption along the melt surface. The sump asymmetry can be adjusted with optimization of the EB power density.

Key words: electron beam cold hearth re-melting; fluid flow; sump evolution; asymmetry temperature distribution

The titanium and titanium alloys have been widely used in aero and space industries. Various processes for consolidation titanium sponge and scrap, for instance, the Electron beam cold hearth re-melting (EBCHR), are adopted in industrial production. Because of the comprehensive respect to prevent low density inclusions (LDI) and high density inclusions (HDI)[1], the EBCHR process has been developed to produce high quality titanium ingots[2-5], especially titanium slab ingot. The schematic of the EBCHR process is shown in Fig.1. The titanium sponge or compressed titanium blocks with alloying elements are transported into the melting hearth where high density power of electron beam is applied to melt raw materials. After melting, molten titanium flows into the refining hearth, where the purification process functions. The pour notch is asymmetrically located in one narrow face of the mold near the refining hearth. The purified melt is solidified in the copper mold; therefore the melting process and solidification process are separated, and this facilitates the purification process. Compared with the vacuum arc re-melting (VAR)[6] process which only produces round ingot, another advantage of the EBCHR process is that it allows producing billet ingot and slab ingot.

TA10 alloy (Ti-0.3Mo-0.8Ni) is a α-type titanium alloy with outstanding corrosion resistance in high temperature and high chloride content conditions. TA10 slab ingots are widely used as raw materials for hot rolling and cold rolling to produce sheet and ribbon, which can reduce production cost significantly. However, defects often occur in such alloy ingot during the EBCHR process.

Top surface power input is an important parameter in EBCHR, and it substantially affects the fluid flow and the

Received date: November 18, 2019
Foundation item: National Key R&D Program of China (2016YFB0301202)
Corresponding author: Shen Houfa, Ph. D., Professor, Key Laboratory for Advanced Materials Processing Technology, Tsinghua University, Beijing 100084, P. R. China, Tel: 0086-10-62789922, E-mail: shen@tsinghua.edu.cn

Copyright © 2020, Northwest Institute for Nonferrous Metal Research. Published by Science Press. All rights reserved.

temperature distribution in the ingot which determine the shape of sump during casting process. In order to improve the ingot quality, researchers[7-10] addressed this issue by investigating various casting process parameters. Because of the asymmetry in geometry of mold, the thermal stress and strain generated in asymmetrical solid shell over the cross section of the ingot are non-equilibrium, and the ingot distortion may occur. McClelland[11] developed a finite element model to describe the pool shape of titanium alloy without considering the overflow region and the simulation results could not show the asymmetry of the sump which was proved by the observation of the etched section of ingot. When the ingot is withdrawn out of the mold, the friction in the vicinity of shell surface contacting to the mold influences ingot surface quality. To explore these phenomena, numerical simulation and experiments were carried out. Zhuk[12] proposed that the distribution of EB power input affects the round ingot surface quality directly. Experimental data show that a shallow pool improves the surface quality of titanium alloy ingot. Shuster[13] reported a phenomenon that thermal-driven buoyancy caused by EB power influences the direction of surface fluid flow near the inlet of melt to the mold. Zhao[14] developed a three-dimensional steady state thermal fluid model of billet ingot and numerical simulation results show that energy loss from the top surface is dominant which accounts for 31%. Gao[15] found that the electron beam pattern maintained the temperature on the molten surface with a gentle temperature gradient when beam-frequency was 5 Hz. The width and depth of molten pool increase gradually with the increase of EB power when melting vanadium[16]. The non-contact method is often used to measure the temperature of molten metal in vacuum furnace[17-19]. All of these works focused on thermal fluid in round ingots and billet ingots. So far only a few works have been done on modeling of the asymmetrical fluid flow and solidification in the slab ingots during the EBCHR process. It is known that the fluid flow in the slab ingot is more special compared with that in the round or billet ingots because of the geometrical factors. Study of the coupling of fluid flow and heat transfer in slab ingot is still worthy to reveal the relationship between the EB power input and the sump profile, especially at the transient start-up stage, and the work will contribute to optimizing EB power input for improving ingot quality.

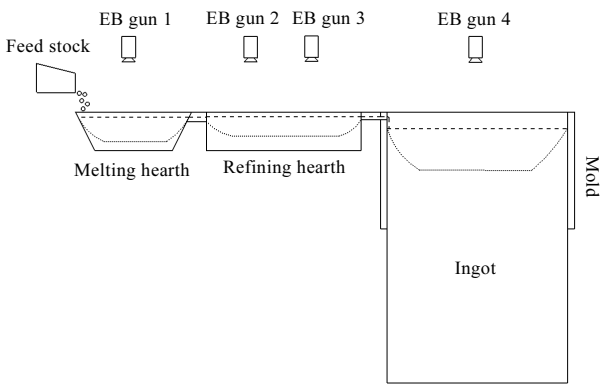

Fig.1 Schematic of electron beam cold hearth re-melting process

In this work, the Mixed Lagrange and Euler (MiLE) approach was employed to simulate the unsteady solidification process and sump evolution at the initial period of EBCHR casting. A set of power input strategies were designed to investigate the fluid flow, temperature distribution and sump profile within the mold.

1 Mathematical Model

1.1 Governing equations

The continuity equation, momentum equation and energy equation were applied in the modeling of fluid flow and solidification during the EBCHR process. The mass conservation equation is:

$$\frac{\partial \rho}{\partial t} + \nabla \cdot (\rho \boldsymbol{u}) = 0 \tag{1}$$

where ρ is the density of alloy, t is time, $\boldsymbol{u}$ is the vector of fluid velocity. The density depends on the temperature and is described as following linear approximation:

$$\rho = \rho_0[1 - \beta_T(T - T_{ref})] \tag{2}$$

where ρ_0 is the density at reference temperature, β_T is the thermal expansion coefficient, T is temperature, T_{ref} is the reference temperature. The momentum equation is:

$$\rho \frac{\partial \boldsymbol{u}}{\partial t} + \frac{\rho}{g_l}\nabla \cdot (\boldsymbol{u} \times \boldsymbol{u}) = \nabla \cdot (\mu \nabla \boldsymbol{u}) - g_l \nabla p + g_l \rho g - \frac{\mu}{K} g_l \boldsymbol{u} \tag{3}$$

where g_l is the liquid fraction, μ is the dynamic viscosity, p is the static pressure, g is the gravity vector, and K denotes permeability. The energy equation is:

$$\rho \frac{\partial H}{\partial t} + \rho c_p \boldsymbol{u} \cdot \nabla T = \nabla \cdot (\lambda \nabla T) \tag{4}$$

where λ is the thermal conductivity, c_P is the specific heat, H is the enthalpy and is depicted as:

$$H(T) = \int_0^T c_P \mathrm{d}T + L(1 - f_S) \tag{5}$$

where L is the latent heat, f_S if the fraction of solid.

Enthalpy method was used to deal with latent heat of solidification.

1.2 Modeling and materials properties

The mold has an internal cross-section of 1050 mm×210 mm with a pour notch located in one narrow face. The length of the ingot is 1050 mm, while half thickness is 105 mm, and the maximum height is 1400 mm. During the modeling of transient start-up process, the calculation domain was enlarged. Euler mesh of 20 mm height was set as “up do-

main" and Lagrange mesh of 20 mm height was set as "down domain" for unsteady state analysis. 0~100 accordion layers with each layer height of 10 mm were set between the up domain and the down domain as the ingot was pulled. To simulate the withdrawal process of ingot, the accordion layers were unfolded one by one till the end of simulation. A periodic boundary condition was applied in the interface between the up domain and the down domain. Considering the size of the pour notch and casting speed of slab, the inlet was set to be a rectangle of 20 mm×20 mm. The thermal properties of TA10 alloy for simulation were calculated in ProCAST database by Lever model of local solute redistribution equation during solidification. All these properties were temperature dependent, with the solidus of 1579 °C and the liquidus of 1657 °C.

1.3 Power input on melt top surface

The scanning frequency of electron beam is high enough and the EB power can be treated as stable, so heat flux was used to represent EB gun power on the melt surface. For applying a distinct power input, the top surface was sectioned to 2 equivalent zones along the length of the mold. The zone near the inlet was named as Zone 1 and the one opposite to the inlet was named as Zone 2. Considering the losses of electron beam power by scattering[20, 21], absorption factor was set to be 0.7. The emissivity of liquid metal was set to be 0.4 in the vacuum environment of the furnace. Table 1 lists the power density in the two zones and the total EB power input on top surface. These power inputs were arranged as 8 cases, in which Case 1 to Case 3 were set to analyze the industrial production while Case 4 to Case 8 were set for studying the pool sump evolution under different total EB powers.

1.4 Boundary and initial conditions

The pouring temperature of the liquid metal in the mold was set at 1900 °C with a superheat of 243 °C. The casting speed was set to be 0.2 mm/s. The vertical inlet metal velocity was assumed to be 71.9 mm/s, which was calculated according to the ratio between the inlet surface area and the slab cross section. The heat transfer coefficient between the mold and the ingot was determined according to the practice and the references data[13, 14, 22-24], which was determined by a function of the air gap thickness, varying from 500 W/(m^2·K) at the melt top to 30 W/(m^2·K) at the mold bottom. Low heat transfer coefficient was applied between the ingot and the mold because the internal face of the mold was rough and covered with titanium film by the deposition of titanium vapor. Air gap between the ingot and the mold formed rapidly due to the shrinkage of solidified ingot.

Heat transfer coefficient in the region below the mold was equal to constant 10 W/(m^2·K). Heat transfer coefficient between the ingot and the bottom block was set to be 500 W/(m^2·K) because of the firm contact and water cooling of the bottom block. Mold was assumed to be at room temperature of 25 °C.

Table 1 Power density in two zones and total EB power input on top surface of ingot

Case	Power density/kW·m^{-2}		Total EB power/kW
	Zone 1	Zone 2	
1	790	790	250
2	630	950	250
3	950	630	250
4	500	500	159
5	600	600	190
6	700	700	222
7	800	800	255
8	1000	1000	316

2 Results and Discussion

2.1 Stability and asymmetry of the pool sump

Fig.2 shows the variation of the sump depths at three positions along the slab length x with time in Case 1 of Table 1. It can be found that the sump becomes deeper with the time going, and finally the depths turn to be steady after 2500 s with symmetrical power density of 790 kW/m^2.

It should be noted that the position x=525 mm in Fig.2 is at the middle length of ingot, while x=100 mm and x=950 mm are at symmetrical positions along the length. From Fig.2, it can be found that the sump depth near the inlet at x=100 mm is deeper than that opposite to the inlet at x=950 mm from 500 s to 1500 s. The deviation of the sump depth at two symmetrical points is about 15 mm in this period. It is estimated that the flow infiltration is attributed to illustrate this phenomenon. When the fluid flows into the mold from inlet near the narrow face, the shell of ingot is remelted and infiltrated by the high temperature fluid. More details are analyzed in the following.

2.2 Fluid flow and temperature distribution

Fig.3 shows the instantaneous streamline and the velocity magnitude of fluid flow along the vertical section of the ingot paralleled to the large face at 3000 s of three cases, in

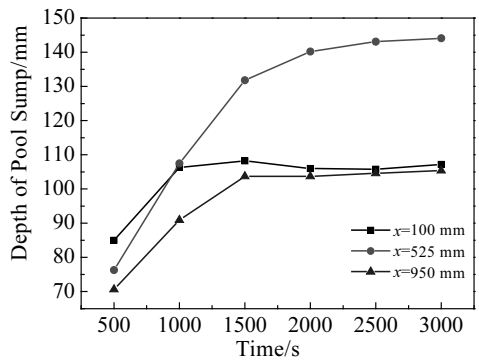

Fig.2 Sump depth along slab length at x=100, 525, 950 mm with casting time in Case 1

which Fig.3a is Case 1 in Table 1 with uniform power input on the melt top surface, while Fig.3b is Case 2 with low energy density near the inlet and Fig.3c is Case 3 with low energy density away from the inlet. The total EB power input on the melt surface of Case 1 to Case 3 is the same as 250 kW. Each case similarly reveals that the fluid from the inlet rebounds quickly after pouring into the mold in Zone 1. When the EB power density on Zone 1 is 790 kW/m^2 in Case 1 or 630 kW/m^2 in Case 2, the pouring fluid infiltrates into the liquid metal and rebounds with the impinging depth of 90 mm as shown in Fig.3a and Fig.3b. When the EB power density is 950 kW/m^2 on Zone 1 in Case 3, the impinging depth of the rebounded flow is about 50 mm as shown in Fig.3c which is shallower than that in Case 1 and Case 2. The streamline in Fig.3a shows that the main fluid in Case 1 moves horizontally along the melt top surface in Zone 1 and goes down at the position x of 600 mm in Zone 2. Fig.3b shows that the main fluid in Case 2 moves horizontally under the melt surface and goes up at the position A where x is about 700 mm. The rebound of inlet fluid can be explained with the density difference of the entering hot melt relative to the surrounding cold melt. With higher input energy, the melt surrounding the inlet fluid should be hotter and it will be early rebounded. Comparing the fluid flow in Case 1 and Case 2, it can be found that the main fluid with higher input power and low density is likely to keep moving on surface while the fluid with lower input power and high density is likely to go down. The density of main fluid in Zone 1 in Case 3 is the lowest because the EB power density is the highest of 950 kW/m^2, so the main fluid keeps moving on the melt top surface at Zone 1 and Zone 2. With the high EB power density at the zone near inlet, the solidifying shell is slightly infiltrated by the inlet flow. When the EB power density is uniform (Case 1), the sump is approximately symmetrical after casting for 3000 s. When the EB power density is 630 kW/m^2 in Zone 1 and 950 kW/m^2 in Zone 2 (Case 2), the sump in Zone 2 is slightly deeper than that in Zone 1. When the EB power density is 950 kW/m^2 in Zone 1 and 630 kW/m^2 in Zone 2 (Case 3), the sump in Zone 1 is obviously deeper than that in Zone 2.

The distinctive fluid flow on the melt top surface of ingot in Case 1 to Case 3 is illustrated in Fig.4. The backward fluid flow (with the direction pointed to the inlet) meets the forward flow (with the direction opposite to the inlet) and then leads that the forward flow is forced to go down in Case 1 (Fig.3a and Fig.4a), while the forward flow is forced to go up in Case 2 (Fig.3b and Fig.4b). This phenomenon often happens in slab casting for the sake that the forced flow is likely to concentrate in a rectangular mold rather than in the round or square mold. Fig.4c shows that the flow enforced by the high density power near the inlet is much stronger and keeps forward along the melt top surface. The mean surface velocity is 50 mm/s when EB power density in Zone 1 is 950 kW/m^2 (Case 3).

Temperature distribution on the melt top surface with different power input is presented in Fig.5. Fig.5a shows that the surface temperature increases from Zone 1 to Zone 2 with homogeneous EB power density in Case 1. Compared to the surface temperature on Zone 2 up to 1900 °C, the surface temperature on Zone 1 is about 1880 °C, with a difference of 20 °C, as shown in Fig.5a. This phenomenon can be certificated by the observation of brighter top surface on Zone 2 during the practical operation, and it can be explained by the surface power input and the heat transportation. In Zone 1, the fluid flow on the melt top surface is strong enough to transfer heat efficiently and therefore heat concentration rarely emerges in Zone 1. Another reason for the surface temperature on Zone 1 which is lower than that on Zone 2 is that the fluid with low temperature rises in Zone 1 (Fig.3 and Fig.4). When the EB power density is lower on Zone 1, the surface temperature is much lower in Case 2 as shown in Fig.5b. In Fig.5b, a regular boundary line forms at the middle length of slab (x=525 mm). This illustrates that the weak fluid flow exists at the middle length where the heat is hardly transported by fluid flow. The tendency of

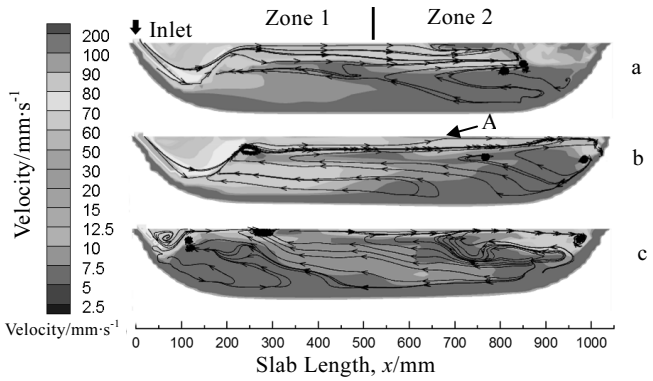

Fig.3 Streamline and velocity magnitude in central vertical section of ingot in Cases 1 (a), 2 (b) and 3 (c)

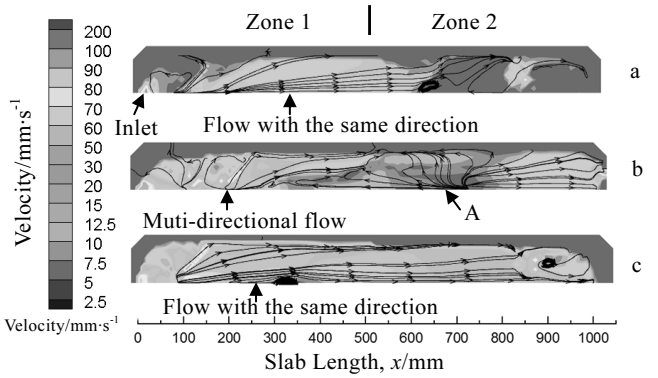

Fig.4 Streamline and velocity magnitude on the top surface of ingot in Cases 1 (a), 2 (b) and 3 (c)

temperature variation in Case 2 means that the descent of mean fluid velocity on the top surface leads to heat concentration because of attenuated flow with poor capacity to transfer heat. Fig.5c shows the surface temperature distribution with higher EB power density on Zone 1 in Case 3. In Case 3, due to the raised flow, surface temperature on Zone 1 is near to that of the inlet and then gradually increases to 1950 °C at middle length, which is the highest in three cases. The tendency of temperature variation in Case 3 means that the flow concentrates on the melt top surface and also leads to heat concentration because the EB power is just transferred on melt top surface and the surface temperature increases along with the mold length. During the EBCHR process, higher surface temperature leads to more melt evaporation. Considering the three strategic distributions, Case 2, i.e., lower power density near the inlet, is not recommended for casting titanium alloys due to the weak fluid flow and the high surface temperature in Zone 2.

In order to verify the reliability of temperature simulated, a laser thermometer was used to measure the surface temperature of melt in the mold. The precision of thermometer was firstly tested by measuring the interface temperature between the liquid titanium and solid titanium. Surface temperature on the melt was then checked in four regions with each size of 5 × 5 mm as shown in Fig.6. The result show that the surface temperature near inlet is lower than that away from the inlet. The measured temperature from region 1 to region 4 is 1870, 1879, 1920 and 1987 °C, respectively, which is in accordance with the simulation results of 1875, 1885, 1935 and 1950 °C in Fig.5a.

2.3 Influence of the power input

Fig.7 presents the sumps at steady state with different EB power densities (Case 4 to Case 8 in Table 1). With the increase of power density, both the size and the depth of sump increase. When the power input density is low (e.g. 500 kW/m^2 in Case 4), the top surface melt solidifies before it reaches the narrow face opposite to the inlet. In Case 4, the sump is very shallow because of low EB power input. Besides, the sump in Case 4 is most asymmetrical due to the interaction of fluid flow and heat transfer caused by the inlet position. The forward flow on the melt top surface transfers heat to the zone opposite to the inlet, and this makes the sump in Zone 2 deeper.

Fig.8 shows that the depth of the sump at the middle width of slab varies with EB power input at 3000 s when the sump depth is stable. The sump depth does not increase proportionally but asymptotically with the power input because of nonlinear increasing of the radiation on melt top surface and the heat transfer through the side wall of ingot. Fig.9 shows the sumps in the central vertical section of slab at steady state. When the EB power density is 700 kW/m^2, the sump depth near the inlet is deeper than that opposite to the inlet (Case 6). When the EB power density is equal to 800 kW/m^2, the sump is near to be symmetrical (Case 7). When the EB power density is equal to 1000 kW/m^2, the sump depth near the inlet is shallower than that opposite to the inlet (Case 8).

Therefore, it can be understood that the sump is affected by

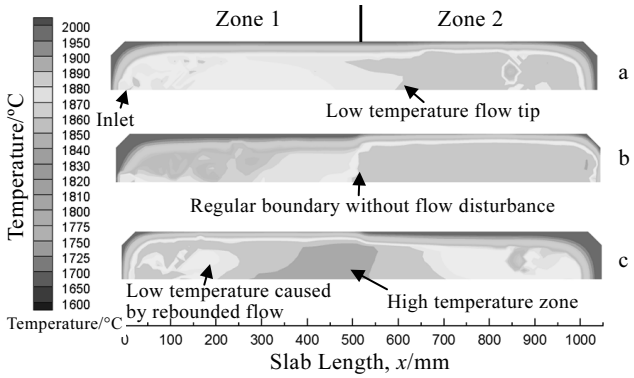

Fig.5 Temperature distribution on melt top surface in Case 1 (a), Case 2 (b), and Case 3 (c)

Fig.6 Regions for temperature measurement with different slab lengths (x =150, 400, 650, 900 mm)

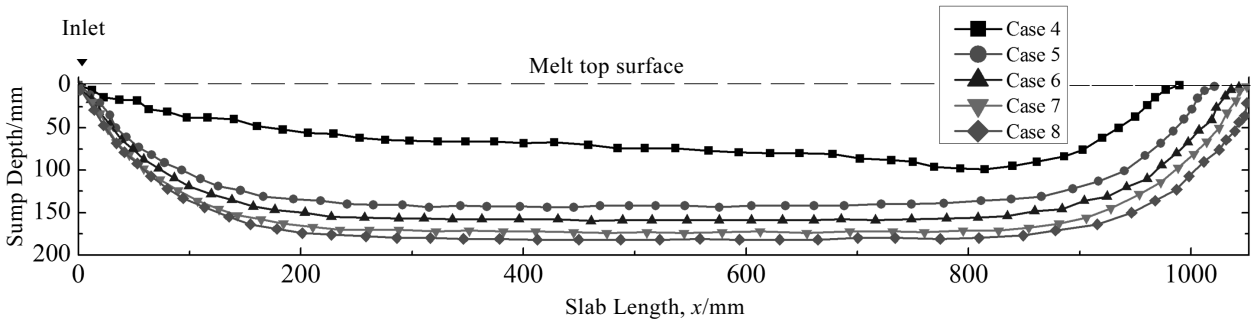

Fig.7 Comparison of sumps at steady state along the central vertical section with symmetrical power input (Case 4 to Case 8 in Table 1)

the fluid flow and heat transfer within the asymmetrical mold. The EB power density, pouring temperature and flow infiltration codetermine the symmetry of sump. The inlet fluid may infiltrate in the solidifying shell because of the inertia, and it can also rebound to the melt surface because of the buoyance. Both the infiltration and rebounding affect heat transfer and finally determine the sump profile. EB power distribution limits the overflow submersing in the mold by heating up the melt upon surface. High temperature flow heated by high density EB power rises rapidly when encountering the low temperature melt underneath the melt top surface. When the EB power density is low, flow infiltration and heat from pouring melt reduce the shell thickness near inlet and generate a deeper sump than another side. When the EB power density is high, heat from surface absorption is significantly lower than that from pouring melt. So the sump depth opposite to the inlet is deeper than that near the inlet because of the surface heat absorption, and heat concentration forms on the melt top surface at the zone opposite to the inlet due to the weak fluid flow.

2.4 Optimization of the EB power distribution

In order to attain a symmetrical sump in whole period of the EBCHR process, a power input distribution was suggested in Table 2. EB power was applied on the melt surface in four zones as shown in Table 2, and the total EB power was calculated with 250 kW for the slab cross section of 1050 mm×210 mm. Fig.10 shows the sump depth with the optimized power input. The maximum deviation of the sump depth at x=100 mm and x=950 mm is about 5 mm after casting for 500 s, which is significantly lower than that in Case 1 with uniform EB power distribution at the melt top surface. Increasing the power input density near the two mold narrow faces leads to two different effects. The first is that the high EB power density near inlet enforces the input flow to keep moving on the melt surface and this consequently decreases the fluid infiltration in the solidifying shell. The second is that the high EB power density away from inlet provides more heat and leads to a deeper sump. These effects balance the sump depth and make the pool more symmetrical. The practice in production indicates the effectiveness of the optimization.

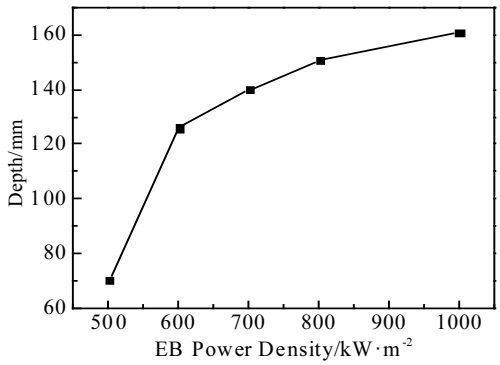

Fig.8 Variation of sump depth at steady state along the middle width of slab (x=525 mm) with the EB power density

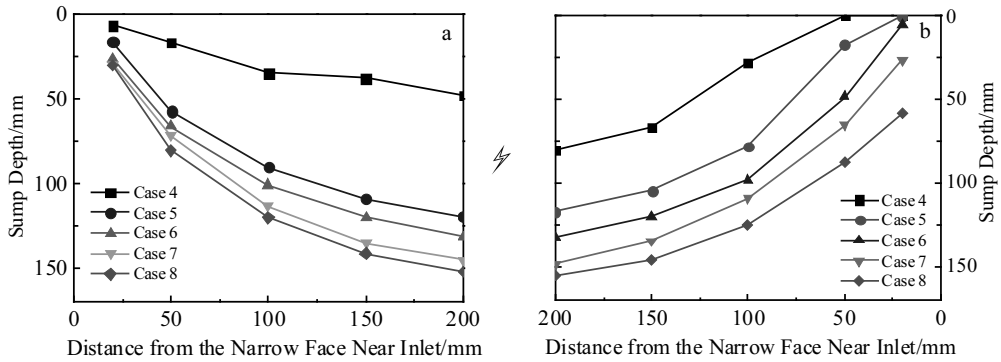

Fig.9 Sumps in the central vertical section of slab from Case 4 to Case 8 in Table 1: (a) near inlet and (b) away from inlet

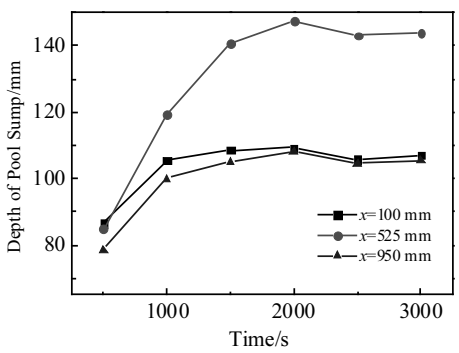

Fig.10 Sump depth along the different slab lengths with casting time after the optimization of the power input in Table 2

Table 2 Optimization of the power input distribution in EBCHR of slab

Zone length/mm	0~262.5	262.5~525.0	525.0~787.5	787.5~1050.0
Power density/kW·m^{-2}	880	720	720	880

3 Conclusions

1) The sump depends on the casting time and turns to be steady at 2500 s for a typical industrial production of TA 10 slab with cross section of 1050 mm×210 mm and casting speed of 0.2 mm/s.

2) The sump is asymmetrical before 2000 s with identical EB power density of 790 kW/m^2. The deviation of the sump depth is 15 mm at two symmetrical points of 100 mm apart from the mold edges. The depth of sump at the steady state increases with the increase of total power input.

3) The asymmetrical sump is induced by the coupling of fluid flow and heat transfer within the asymmetrical mold during the EBCHR. The temperature distribution on the melt top surface is asymmetrical even with homogeneous EB power density. The inlet flow infiltrates or rebounds according to the inertia and buoyance of fluid. The infiltration of downward inlet flow reduces the solidifying shell especially at the startup of casting, while the rebound of upward inlet flow enforces the heat absorption along the melt surface.

4) The sump asymmetry can be adjusted with optimization of the EB power density by decreasing the flow infiltration near the inlet and balancing the heat away from the mold inlet. The deviation of sump depth is less than 5 mm at two symmetrical points during the startup of casting with optimization of the EB power density. Applying high density power near the inlet leads to strong flow on the melt top surface with the direction opposite to the inlet, while applying low density power near the inlet keeps the poured melt moving underneath the melt top surface.

References

1 Cen Mengjiang, Liu Yuan, Chen Xiang *et al. China Foundry*[J], 2019, 16(4): 223

2 Mitchell A. *Materials Science and Engineering A*[J], 1998, 243: 257

3 Suzuki H G , Eylon D. *Materials Science and Engineering A*[J], 1998, 243: 126

4 Kanayama H, Kusamichi T, Muraoka T *et al. ISIJ International*[J], 1991, 31(8): 906

5 Gorgul S I, Medvedev M I, Bespalova N A *et al. Metallurgist* [J], 2013, 57(7-8): 748

6 Yang Zhijun, Zhao Xiaohua, Kou Hongchao *et al. Transactions of Nonferrous Metals Society of China*[J], 2010, 20(10): 1957

7 Fjaer H G, Mo A. *Metallurgical Transactions B*[J], 1990, 21B: 1049

8 Du Q, Eskin D G, Katgerman L. *Materials Science and Engineering A*[J], 2005, 413-414: 144

9 Drezet J M, Rappaz M. *Metallurgical and Materials Transactions A*[J], 1996, 27A: 3214

10 Vutova K, Vassileva V, Koleva E *et al. Journal of Materials Processing Technology*[J], 2010, 210(8): 1089

11 McClelland M A, Westerberg K W, Meier T C *et al. Abstract of Papers of American Chemical Society*[C]. California: University of North Texas Libraries, 1997

12 Zhuk H V, Kobryn P A, Semiatin S L. *Journal of Materials Processing Technology*[J], 2007, 190(1-3): 387

13 Shuster R, Reilly C, Maijer D M *et al. IOP Conference Series: Materials Science and Engineering*[C]. Schladming: IOP Publishing Ltd, 2012

14 Zhao X, Reilly C, Yao L *et al. Applied Mathematical Modelling*[J], 2014, 38(14): 3607

15 Gao Lei, Huang Haiguang, Zhang Yuqin *et al. JOM*[J], 2018, 70(12): 2934

16 Su Bin, Chen Daoming, Wang Zhenhong, *et al. Rare Metal Materials and Engineering*[J], 2019, 48(3): 711

17 Kusamichl T, Kanayamaa H, Onoye T. *ISIJ International*[J], 1992, 32(5): 593

18 Loussouarn T, Maillet D, Remy B *et al. 9th International Conference on Inverse Problems in Engineering*[C]. Waterloo: IOP Publishing Ltd, 2017

19 Shang Yonghong, Tao Dongxing, Hou Yaqing *et al. International Conference on Optical Instruments and Technology 2017*[C]. Beijing: Society of Photo-Optical Instrumentation Engineer Digital Library, 2017 (in Chinese)

20 Suzuki K, Watakabe S. *Metals and Materials International*[J], 2003, 9(4): 359

21 Ritchie M, Lee P D, Mitchell A *et al. Metallurgical and Materials Transactions A*[J], 2003, 34a: 863

22 Kobryn P A, Semiatin S L. *Metallurgical and Materials Transactions B*[J], 2001, 32B: 685

23 Katia Vutova, Veliko Donchev. *Applied Mathematical Modelling*[J], 2016, 40(2): 1565

24 Vutova K, Vassileva V and Mladenov G. *Vacuum*[J], 1997, 48(2): 143

电子束冷床炉熔铸 TA10 钛合金非对称流动及凝固过程数值模拟

许耀平[1]，陈其朋[1]，刘　源[1]，史亚明[2]，秦铁昌[2]，沈厚发[1]

(1. 清华大学 材料学院 先进成形制造教育部重点实验室，北京 100084)

(2. 昆明钢铁集团，云南 昆明 651206)

摘　要：熔池中的流动是影响电子束冷床炉熔铸铸锭质量的一个非常重要因素。本研究通过建立三维非稳态模型研究电子束冷床炉熔铸钛扁锭过程中的流动及熔池形态变化，采用混合欧拉-拉格朗日算法模拟非稳态凝固过程。通过设置一系列的能量输入策略，分析了不同电子枪功率下的结晶器内的非对称流动特征、温度场及熔池形态变化。研究结果表明流动及传热共同导致了非对称熔池的形成。钛液从溢流口进入结晶器后，一部分向下流动侵蚀凝固坯壳，一部分由于不同温度的密度差受到的浮力返回了液面。凝固坯壳被侵蚀后变薄影响对称性，返回液面的钛液改变了液面温度，影响了能量吸收效率及液面温度分布。通过优化电子枪的能量输入策略，可以有效的改善熔池的对称性，避免因熔池不对称导致熔铸缺陷的出现。

关键词：电子束冷床炉；流动；熔池变化；非对称温度场

作者简介：许耀平，男，1986 年生，博士生，清华大学材料学院，北京 100084，电话：010-62789922，E-mail: xu1986103315@163.com